Ultrafast Electron Transfer between Molecule Adsorbate and Antimony Doped Tin Oxide (ATO) Nanoparticles

Jianchang Guo, Chunxing She, and Tianquan Lian*

Department of Chemistry, Emory University, Atlanta, Georgia 30322

Received: November 29, 2004; In Final Form: February 4, 2005

Ultrafast transient IR spectroscopy has been used to examine the effect of doping on interfacial electron transfer (ET) dynamics in Re(dpbpy)(CO)$_3$Cl (dpbpy = 4,4′-(CH$_2$PO(OH)$_2$)2−2,2′-bipyridine) (ReC1PO$_3$) sensitized ATO (Sb:SnO$_2$) nanocrystalline thin films. In films consisting of particles with 0%, 2% and 10% Sb dopant, the rates of electron injection from the adsorbate excited state to ATO were independent of and the rates of the recombination increased with the doping level. The observed similar forward electron injection rates were attributed to negligible changes of available accepting states in the conduction band at the doping levels studied. The dependence of the recombination rate on conduction band electron density and a possible mechanism for the recombination process were discussed.

Introduction

Photoinduced electron transfer (ET) between molecular adsorbates and semiconductor nanoparticles has been a subject of intense interest in recent years.[1,2] This process is involved in photovoltaic devices based on molecule/nanoparticle composites, such as dye sensitized semiconductor,[3,4] and quantum dot/conjugated polymer solar cells.[5] A high conversion efficiency in these solar cells requires a fast charge separation across the molecule/nanoparticle interface and a much slower charge recombination.[6,7] In Ru polypyridyl dye sensitized TiO$_2$ nanocrystalline thin films, the major component in the most efficient dye-sensitized solar cell reported so far, both ultrafast injection[8−19] and slow recombination[14,20−30] have been observed. Similar studies have also been extended to other semiconductors (such as SnO$_2$,[13,31−34] ZnO[16,35−38] and Nb$_2$O$_5$[39]) in an effort to understand how electron injection and recombination dynamics depend on the properties of semiconductors.

Transparent conducting glass electrodes, consisting of glasses coated with doped wide band-gap semiconductor thin films, such as Sb:SnO$_2$ (ATO), F:SnO$_2$ (FTO) and Sn:In$_2$O$_3$(ITO), have been extensively used in polymeric and molecular photovoltaic devices[3,4,40−46] due to their high conductivity and transparency. However, to our knowledge, the charge separation and recombination dynamics at their interface with molecules have not been reported. It is unclear how they differ from those of the corresponding undoped semiconductor such as SnO$_2$ (for ATO). In the simplest consideration, doping increases electron density in the materials and raises the Fermi level to a higher energy (or more negative potential). The effect of Fermi level change on charge transfer dynamics has been investigated previously in Ru bipyridyl-sensitized TiO$_2$ by varying external bias.[21,47] It was shown that with increasing negative bias, the rate of injection was retarded and the rate of recombination was enhanced.

In this paper, we report a study of the effect of doping on the electron injection and recombination dynamics in Re(dpbpy)-(CO)$_3$(Cl) [dpbpy = 2,2′-bipyridine 4,4′-CH$_2$−PO$_3$H$_2$] (ReC1PO$_3$) sensitized ATO nanocrystalline thin films. We utilized transient

CHART 1: Schematic Structure of Re(dpbpy)(CO)$_3$Cl (dpbpy = 4,4′-(CH$_2$PO(OH)$_2$)$_2$−2,2′-bipyridine) (ReC1PO$_3$)
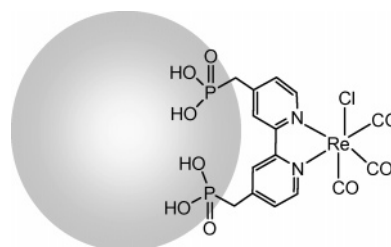
mid-IR spectroscopy to investigate the forward and back electron-transfer rate of ReC1PO$_3$ on ATO films with different antimony doping level. The ReC1PO$_3$ dye was chosen because its strong CO stretching modes could be monitored to follow the change of ground state, excited state, and cation, similarly to Re(dcbpy)(CO)$_3$Cl [dcbpy = 2,2′-bipyridin-4,4′-CH$_2$−COOH] (ReC1A), used in previous studies.[32,48,49] Furthermore, both the injection and back recombination rates are faster in ReC1PO$_3$ than those in ReC1A, allowing a more reliable determination of recombination rate in our <1 ns observation window. The doping level is controlled synthetically by the addition of a different amount of Sb and the resulting electron density in the conduction band is determined from the IR absorption spectrum of the free carriers according to Drude model.[50−52] At the doping levels examined, the injection dynamics is similar to that in SnO$_2$, but the recombination rate increases with the doping level. Mechanisms of the doping level dependent recombination process are discussed.

Experimental Section

Sample Preparations. Re(dpbpy)(CO)$_3$Cl (dpbpy = 4,4′-(CH$_2$PO(OH)$_2$)$_2$−2,2′-bipyridine) (ReC1PO$_3$) was synthesized by Prof. Hupp's group at Northwestern University according to a published procedure.[30,53] As shown in Chart 1, the complex is believed to attach to the surface of ATO via the PO(OH)$_2$ groups.[30,53]

Colloidal ATO was synthesized according to a published procedure.[54] Briefly, 30 g (∼85 mmol) of SnCl$_4$·5H$_2$O (98%,

* Corresponding author. E-mail: tlian@emory.edu.

from Aldrich) was dissolved in 500 mL of H_2O (Millipore, 18.3 $M\Omega/cm$), to which a solution of $SbCl_3$ (98%, from Aldrich) dissolved in 20 mL of HCl (37 wt %) was added dropwise in an ice bath under rapid stirring. The doping level was controlled by the amount of $SbCl_3$ solution added and two samples with Sb to Sn molar ratio of 0.02:1 and 0.1:1 (referred to as 2% and 10% ATO, respectively) were prepared. After stirring for additional 30 min, aqueous ammonia (25%) was added to the clear solution to adjust the pH to 3.5−4.0, which led to the precipitation of nanoparticles. The solution was allowed to settle overnight in the dark, during which, the color of the white precipitate changed to yellow. The precipitates were washed at least three times with water and then dissolved in 300 mL of water. The solution was adjusted to a pH value of 9.5−10, stirred for more than 8 h, and dialyzed against 10 L of aqueous ammonia at pH 10 to produce clear ATO solution.

The ATO colloidal solution was refluxed for 4 h. A 120 mL aliquot of this colloid was poured into an autoclave and heated at 150 °C for 1 h and at 270 °C for 16 h. The colloid was then concentrated to 60 mL. Then 5 mL of the solution and 2 drops of TritonX-100 (from Aldrich) were mixed and stirred for 1 day. The resulting solution was cast onto sapphire windows, dried in air, and then baked at 400 °C for 1 h in an oven to produce nanoporous crystalline ATO thin films. SnO_2 nanocrystalline thin films were prepared by a previously published method.[55] Finally, the films were submerged in a saturated solution of $ReC1PO_3$ in methanol for 1 h, washed with methanol, and dried in air prior to transient absorption spectrum measurement. The absorbance of $ReC1PO_3$ molecules on SnO_2 and ATO films was typically 0.2−0.4 OD at 400 nm, corresponding to ∼25−50% of saturated coverage of the films.

Ultrafast Infrared Transient Absorption Measurements. Ultrafast experiments were carried out in a pump−probe transient absorption scheme and the details of the setup have been reported previously.[49,56] Briefly, the tunable infrared spectrometer used for these studies utilizes a 1 kHz regeneratively amplified Ti:sapphire laser system (800 nm, 100 fs, 900 μJ/pulse). Difference frequency generation of the signal and idler output of an IR optical parametric amplifier (OPA) produced the tunable mid-IR probe pulses, which had a ∼250 cm^{-1} bandwidth. Pump pulses at 400 nm were produced by second harmonic generation (SHG) from 800 nm pulses in a BBO crystal. The typical energies of pump and probe pulses were ∼3 μJ/pulse and 0.01 μJ/pulse and their beam diameters at the sample were ∼600 μm and 300 μm, respectively.

The probe was dispersed in a spectrometer and detected with a 32-element MCT array detector. The spectral resolution was 15 nm (∼6 cm^{-1} at 2100 cm^{-1}). Zero time delay and the instrument response were determined in a thin film of CdS nanoparticles, which gave an instantaneous mid-IR absorption response after excitation at 400 nm. Typically, the instrument response at the sample was well fit by a Gaussian function with 160 fs full-width-at-half-maximum (fwhm). During the data collection, samples were constantly translated at a speed around 5 mm/min to avoid permanent damage.

Results

X-ray diffraction (XRD) patterns of SnO_2, 2% ATO, and 10% ATO are shown in Figure 1. The peak positions of these ATO samples agree well with the diffraction of rutile SnO_2 crystals, consistent with the results of previous studies.[54,57] It was demonstrated by Sb K-edge extended X-ray absorption fine structure measurements (EXAFS) that Sb atoms were well
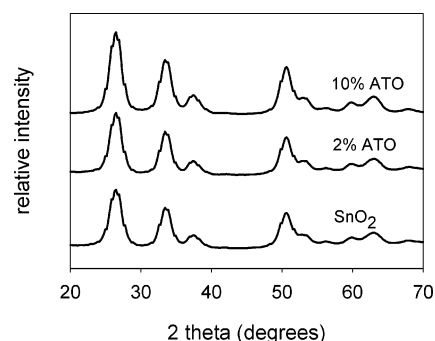

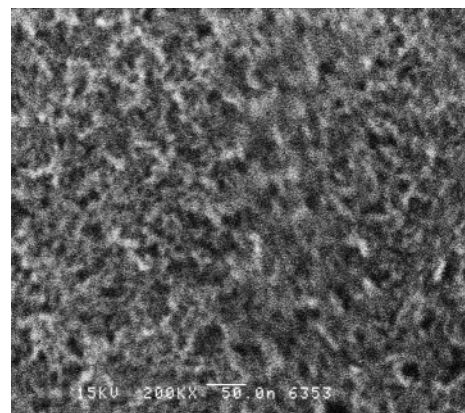**Figure 1.** XRD patterns of SnO_2, 2% ATO and 10% ATO nanoparticles.

Figure 2. A SEM image of a 2% ATO nanocrystalline thin film.

incorporated into the SnO_2 crystalline structure even at 16.7 atomic % antimony doping level.[54] Hence, hereafter, we assume that all doped antimony atoms are also well incorporated into the SnO_2 lattice in our films. Scanning electron microscopy (SEM) images showed that undoped SnO_2, 2% ATO and 10% ATO films were nanoporous, consisting of interconnected nanoparticles with ∼5 nm diameters. The SEM image of 2% ATO film is presented in Figure 2 as an example.

The UV−vis and FTIR absorption spectra of SnO_2 and 2% and 10% ATO films are shown in Figure 3. They consist of a strong valence-to-conduction band transition at <360 nm and a broad IR absorption band, which is centered at ∼3.3 and ∼2.5 μm for 2% and 10% ATO, respectively. The undoped SnO_2 film shows a much weaker IR band centered at ∼3 μm, which was attributed mostly to the adsorbed water.[51] The SnO_2 and 2% ATO films showed no noticeable absorption features between 0.4 and 1.1 μm. In the 10% ATO film, the tail of the IR band centering at 2.5 μm extends to and results in significant absorption in the visible and near-IR region. These IR bands were previously assigned to plasmon bands of the doped electrons and were shown to be well described by the classical Drude model of free electron gas,[51] from which the conduction band electron densities of ATO films could be obtained. The dashed and dotted lines in the right side of the figure show the fitting results using this model, the details of which will be discussed later. The UV−visible spectra of $ReC1PO_3$ on 10% ATO film (dash−dotted line) and in methanol solution (dashed line) are shown in the inset of Figure 3. $ReC1PO_3$ on ATO shows a metal-to-ligand charge-transfer band at 360 nm, similar to its position in methanol solution.

To study the effect of doping on the electron injection and recombination kinetics between adsorbate and ATO films, we compare $ReC1PO_3$ sensitized SnO_2, 2% ATO and 10% ATO. Similar to ReC1A used in previous studies,[32,48,49] $ReC1PO_3$

ET Dynamics in Re(dpbpy)(CO)$_3$Cl

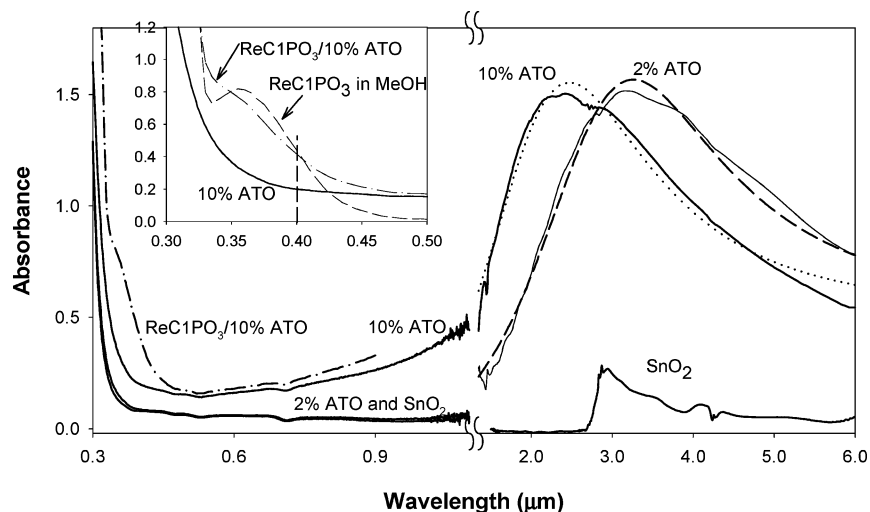*J. Phys. Chem. B, Vol. 109, No. 15, 2005* **7097**

Figure 3. Absorption spectra of naked SnO$_2$, 2% ATO and 10% ATO films (solid line) from 0.3 to 6 μm. The UV−vis and FTIR spectra are collected in two different spectrometers, leaving a small gap between 1.1 and 1.35 μm. The dotted line and dashed line in the right side of the figure are simulated plasmon band absorption spectra (based on Drude model) of 10% and 2% ATO, respectively. The dash−dotted line in the left side shows the UV−vis spectrum of ReC1PO$_3$/10% ATO. An expanded view of UV−vis spectra of ReC1PO3 on 10% ATO (dash−dotted line), naked 10% ATO film (solid line), and ReC1PO$_3$ in methanol solution (dashed line), is shown in the inset.

shows two CO stretching bands at 1930 and 2036 cm^{-1} with the lower frequency band composed of two poorly resolved CO stretching modes. Hereafter, we will focus our discussion on the higher frequency mode to avoid the complexity of such spectral overlap. Optical excitation of the metal-to-ligand-charge-transfer (MLCT) band at 400 nm promotes an electron from a Re d orbital to the π* orbital of the bipyridine, from which electron transfer into ATO occurs.[29,32,48−60]

Transient IR difference spectra of ReC1PO$_3$ on 10% ATO in the higher frequency CO stretching mode region are shown in Figure 4. These spectra are averaged over about 10 delay times in the selected time delay windows: 0.5−1, 2−10, 15−50, 150−350 and 400−800 ps. The raw data are shown in panel a. All the spectra exhibit a broad absorption in the entire region with three narrower vibrational features from the higher frequency CO stretching mode of the adsorbate. The broad signal is assigned to the change of free electron absorption resulted from the injected electrons, as detailed in the earlier section and shown in Figure 3. It reaches its maximum value at ∼15−50 ps and decays subsequently. The narrow vibrational features at 2044, 2059, and 2092 cm^{-1} are attributed, following the assignment of the related ReC1A spectra on SnO$_2$ and TiO$_2$,[32,48,49] to the higher frequency CO stretching band in the ground, excited and oxidized states, respectively.

To better compare the evolution of different vibrational features, we have displaced the spectra at different time delays vertically in panel b. Also included is a transient difference spectrum of ReC1PO$_3$ on ZrO$_2$, which consists of only the ground and excited-state peaks. No oxidized peak is present in this case, because the higher conduction band edge position of ZrO$_2$ prohibits electron injection from the adsorbate excited state.[49] The initial size of the ground-state bleach at ∼2044 cm^{-1} for ReC1PO$_3$/10% ATO is about 2 mOD, which, compared to the ∼0.2 OD static absorbance of the CO stretching band, suggests a ∼1% excitation level under the current experimental condition. The size of the bleach decreases by >50% at later time delays. Unfortunately, there is a significant spectral overlap between this bleach and the oxidized state absorption bands of the lower frequency CO stretching modes, hindering a quantitative analysis of the recovery kinetics. This overlap is also responsible for the slight variation of the bleach band shape
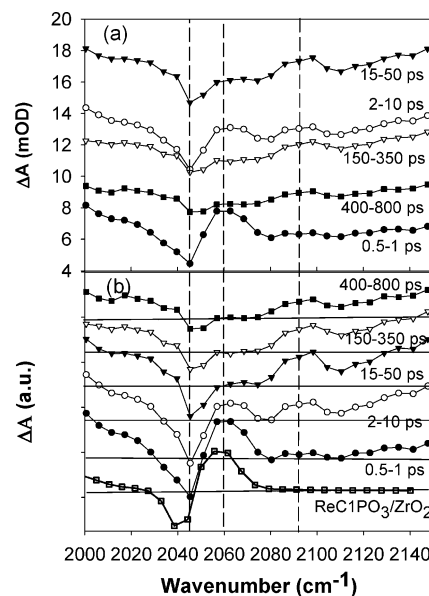

Figure 4. (a) Transient IR absorption spectra of ReC1PO$_3$/10% ATO at 0.5−1 ps (solid circle), 2−10 ps (open circle), 15−50 ps (solid triangle), 150−350 ps (open triangle), and 400−800 ps (solid square) after 400 nm excitation. In addition to the broad IR absorption of injected electrons, the spectra also consist of a bleach of the higher frequency CO stretching mode in the ReC1PO$_3$ electronic ground state (∼2044 cm^{-1}) and its corresponding peaks in the excited state (∼2060 cm^{-1}) and oxidized form (2092 cm^{-1}). (b) Same spectra as in (a) but vertically displaced for a better comparison of vibrational features. Also shown in (b) is a transient spectrum of ReC1PO$_3$ on a noninjecting substrate, ZrO$_2$, at 10 ps, in which only the ground and excited features are observed.

and position at different delay times. Within 15−50 ps, the excited-state peak at 2059 cm^{-1} decays almost completely, coinciding with the formation of the oxidized state peak at 2092 cm^{-1}, indicating that electron injection is the main pathway for excited-state decay. The subsequent decay of the oxidized peak and the recovery of ground-state bleach in the 50 ps to 1 ns time scale suggest charge recombination between the conduction band electrons and dye cations. Similar spectral evolutions are observed for ReC1PO$_3$ on 2% ATO and SnO$_2$.
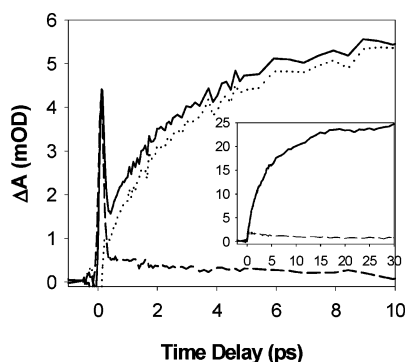
Figure 5. Comparison of transient IR signals at $2120-2150$ cm^{-1} of naked (dashed line) and ReC1PO$_3$ sensitized (solid line) nanocrystalline thin films of 10% ATO. The dotted line shows the kinetic trace of ReC1PO$_3$/10% ATO after subtracting the signals from the naked film. The spike in the early time delays is attributed to the excitation of the plasmon band, which is not present in 2% ATO or SnO$_2$. Shown in the inset are the kinetic traces for ReC1PO$_3$ sensitized (solid line) and unsensitized (dashed line) 2% ATO.

Figure 6. Comparison of absorptions of injected electrons (solid line, averaged value from 2120 to 2150 cm^{-1}) and oxidized adsorbates (solid dot, integrated peak area from 2076 to 2110 cm^{-1}) as a function of time for ReC1PO$_3$ on (a) SnO$_2$ and (b) 10% ATO. The inset in each figure shows an expanded view of the early time dynamics. The injected electron and oxidized dye signals agree well at all time delays, indicating that either one can be used to monitor the electron-transfer dynamics.

To ensure that the broad electron absorption signal contains only contributions from injected electrons, we compare the sensitized and unsensitized films under the same excitation power. Naked 2% ATO and SnO$_2$ films show negligible absorbance at 400 nm and excitation at this wavelength led to less than a few mOD transient IR signals, much smaller than the signals in ReC1PO$_3$ sensitized films, as shown in the inset of Figure 5. The kinetic trace is obtained by averaging the absorbance change between 2120 and 2150 cm^{-1}, at which the signal has negligible contribution from adsorbate vibrational bands and is dominated by electron absorption. The small signals from the naked films are attributed to the excitation of valence band electrons to trap states near the conduction band edge. On the other hand, the unsensitized 10% ATO films have significant absorption at 400 nm. Figure 5 compares the transient IR absorption signals (between 2120 and 2150 cm^{-1}) in 10% ATO films with and without the ReC1PO$_3$ sensitizer. The absorption signals on both films exhibit a large spike that decays within 400 fs. After that, only a small (<0.5 mOD) signal is present in the naked film, which has a relative contribution to the total signal size similar to those observed in 2% ATO and SnO$_2$ and is also attributed to the excitation of valence band electrons to trap states near the conduction band edge by the 400 nm pump. The spike at early delay time observed in the 10% ATO is not present in 2% ATO or undoped SnO$_2$. It is tentatively attributed to the direct excitation of the plasmon band of the 10% ATO film by a 400 nm pump pulse, which can generate hot electrons and broaden the plasmon band.[61-63] The relaxation dynamics of excited plasmon bands in ATO have not been carefully examined, although extensive studies of metal nanoparticles have indicated relaxation times on the picosecond time scale.[61-63] To obtain the kinetics for interfacial ET, the signals from the naked films are subtracted from those of sensitized ones. The subtracted kinetic trace for ReC1PO$_3$ on 10% ATO films is shown in Figure 5 (dotted line). Hereafter, only the subtracted traces, which reflect the kinetics of electron injection and recombination, are presented.

The growth and decay of oxidized peak size shown in Figure 4 appears to correlate with the change of the broad electron absorption signal. The amplitude of the oxidized peak depends on the concentration of the oxidized species, providing a direct probe of the injection and recombination process, whereas the electron signal can be affected by both the change in electron concentration and absorption cross-section. The latter can be
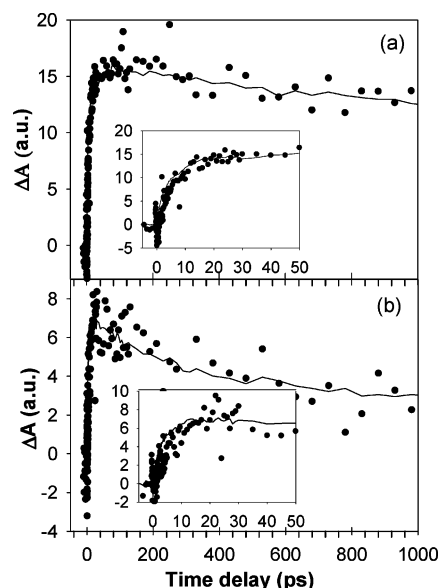
noticeable if the injected electrons undergo substantial relaxation/trapping processes. To quantitatively correlate these species, the temporal evolutions of the oxidized peak area and electron signal are compared in Figure 6a,b for ReC1PO$_3$/SnO$_2$ and ReC1PO$_3$/10% ATO, respectively. The kinetic traces of the oxidized peak are obtained by integrating the peak area between 2076 and 2110 cm^{-1}. Within error, they agree well with those of electron signals after normalization. Similar agreement between electron signal and oxidized peak area is also observed for ReC1PO$_3$/2% ATO (not shown). These agreements indicate that there is negligible absorption cross-section change for the injected electrons in these systems and the IR absorption of electrons can be used to monitor ET kinetics. Because the electron absorption signal is much stronger than the vibrational bands of the oxidized adsorbate, it will be used in the remainder of the paper. Similar approach has been used in previous studies of ReC1A/SnO$_2$,[32] ReC1A/ZnO[36] and RuN3/Nb$_2$O$_5$.[39]

A comparison of electron injection kinetics for ReC1PO$_3$ on SnO$_2$ (dot), 2% ATO (square) and 10% ATO (triangle) is shown in Figure 7a. The signal amplitudes of the injected electrons on these films are different, becoming smaller in films with higher doping level. These traces have been corrected by the absorption of dyes at 400 nm to correspond to the same number of absorbed photons, so their amplitudes reflect the difference in electron injection yields and/or absorption cross-sections. In the next section, we will show that the amplitude difference can be attributed to the doping level dependent electron absorption cross-section in these films. For a better comparison, the kinetics traces of ReC1PO$_3$ on three films are normalized at the maximum (around 50 ps), as shown in Figure 7b. The rise times are similar, but the decay times become faster in samples with higher antimony doping level, suggesting similar forward ET but different recombination rates. The kinetics of ReC1PO$_3$ on SnO$_2$ can be described by biexponential rise, whose time constants and amplitudes (in parentheses) are 2.2 ps (57%) and 15.6 ps (43%), and a slow decay, which reduces the amplitude by 18% at 1 ns. For ReC1PO$_3$/2% ATO the signal decays by
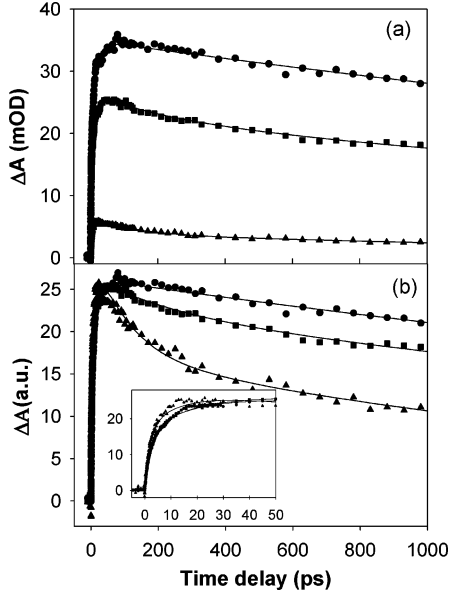
ET Dynamics in Re(dpbpy)(CO)$_3$Cl

J. Phys. Chem. B, Vol. 109, No. 15, 2005 **7099**

Figure 7. (a) Electron injection kinetics (symbols) and fits (lines) obtained by probing electron absorption at 2120−2150 cm^{-1} for ReC1PO$_3$ on SnO$_2$ (solid dot), 2% ATO (solid square) and 10% ATO (solid triangle). The lower panel (b) shows the same kinetic traces after normalizing the amplitude at 50 ps. The inset of panel (b) shows the normalized kinetics at early time delays. The fitting functions are discussed in the text and fitting parameters are listed in Table 1.

TABLE 1: Comparison of Back ET Rates from SnO$_2$ Nanoparticles with Different Sb Doping Levels

semiconductors	N (cm^{-3})	σ (cm^2)	σ_{rel}[a]	A_{rel}[b]	$k_{b,rel}$[c]
SnO$_2$	<10^{18}	~2.8 × 10^{-17}	1	1	0.07
2% ATO	1.85 × 10^{20}	1.9 × 10^{-17}	0.68	0.75	0.15
10% ATO	3.23 × 10^{20}	0.65 × 10^{-17}	0.23	0.2	1

[a] σ_{rel} is the relative electron cross-section. [b] A_{rel} is the relative electron signal size at 50 ps. [c] $k_{b,rel}$ is the relative recombination rate, which is obtained by the fitting procedure discussed in the main text.

about 30% at 1 ns, whereas for the ReC1PO$_3$/10% ATO, the signal decreases by almost 60% at 1ns.

Discussion

Electron Density, Electron Absorption Cross-Section and Fermi Level of ATO Films. Electron density of ATO films can be calculated using the classical Drude model by following the work of Nutz et al.[51] According to the Drude model, we can write the real, ϵ', and imaginary, ϵ'', parts of the dielectric function as[51,64]

$$\epsilon' = \epsilon_\infty - \frac{\omega_N^2}{\omega^2 + \Gamma^2}$$

$$\epsilon'' = \frac{\omega_N^2 \Gamma}{\omega(\omega^2 + \Gamma^2)} \tag{1}$$

where ϵ_∞ is the high-frequency dielectric constant of SnO$_2$, Γ is the damping frequency, and ω_N is related to the conduction band electron density (N) and effective mass (m^*) by

$$\omega_N = \sqrt{\frac{N \cdot e^2}{\epsilon_0 \cdot m^*}} \tag{2}$$

The film is treated as a porous network of nanoparticles embedded in air with a filling factor of f, defined as the volume fraction of nanoparticles in the composite. Using effective medium theory, the extinction coefficient of the plasmon band is given by[51,64]

$$\alpha = f \frac{9\omega\epsilon_m^{3/2}}{c} \cdot \frac{\epsilon''}{(\epsilon' + 2\epsilon_m)^2 + \epsilon''^2} \tag{3}$$

where ϵ_m is the dielectric constant of the embedding medium, assumed to be 1 (for air) in our case. Reflections from the film/air and the film/substrate interfaces are also considered.[51] The filling factor (f), the electron density (N) and the damping constant (Γ), which determine the amplitude, peak position, and width of the plasmon band, respectively, are parameters used in fitting the measured IR spectra. Using $\epsilon_\infty = 3.91$[65] and $m^* = 0.27m_0$,[66] the best fits yield an electron density, filling factor and damping constant of 1.85 × 10^{20} cm^{-3}, 0.21, and 5.55 × 10^{14} s^{-1} for 2% ATO film and 3.23 × 10^{20} cm^{-3}, 0.19, and 8.54 × 10^{14} s^{-1} for 10% ATO film. The dashed and dotted lines in the right-hand side of Figure 3 are fits for 2% and 10% ATO films, respectively, agreeing well with the measured IR spectra.

Using the electron density obtained from the IR spectra, the Fermi level of 2% and 10% ATO films could then be calculated by[67]

$$E_f = E_i + kT \ln\left(\frac{N}{N_i}\right) \tag{4}$$

where E_f and E_i are the Fermi energy of the doped and intrinsic semiconductor, and N_i is the conduction band electron density of the intrinsic semiconductor. E_i is at middle of the band gap. N_i can be calculated by using the band gap energy of the semiconductor, E_g, effective mass of the conduction band electron, m_c, and valence band hole, m_v according to[68]

$$N_i(T) = 2.5\left(\frac{m_c m_v}{m_0^2}\right)^{3/4}\left(\frac{T}{300\ K}\right)^{3/2} \exp\left(-\frac{E_g}{2k_B T}\right)10^{19}\ cm^{-3} \tag{5}$$

Using $E_g = 3.5$ eV, $m_c = 0.27m_0$ and $m_v = m_0$[69] for SnO$_2$, we obtain N_i of ~2.46 × 10^{-11} cm^{-3} at 298 K. Hence, we estimate that the Fermi energy of 2% and 10% ATO is 75 and 90 meV higher than the conduction band edge of SnO$_2$ respectively. Figure 8 shows a schematic diagram of the relevant energy levels of ReC1PO$_3$, SnO$_2$, and 2% and 10% ATO.

From the calculated electron density, N, and the measured extinction coefficient of plasmon band, $\alpha(\lambda)$, determined from the FTIR spectrum, the electron absorption cross-section in ATO films can be calculated by

$$\sigma(\lambda) = \alpha(\lambda)/N \tag{6}$$

The electron cross-sections for 2% and 10% ATO are estimated to be 1.9 and 0.65 × 10^{-17} cm^2, respectively.

It is difficult to determine the electron cross-section of SnO$_2$ using the method above because of the weak plasmon absorption band in SnO$_2$. However, it can be estimated with a few approximations. Because similar methods were used to prepare SnO$_2$ and ATO films, we assume the same filling factor for these films. We further assume that the damping constant for SnO$_2$ is similar to that of 2% ATO. Using these parameters, we can calculate the electron cross-section at different electron density according to eq 6. It is interesting to observe that when the electron density is less than 10^{19} cm^{-3}, the calculated
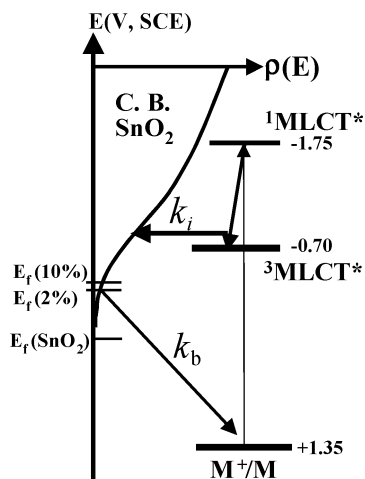
Figure 8. Schematic diagram of relevant energy levels involved in the electron injection and recombination in ReC1PO$_3$ sensitized ATO nanoparticles. The left side depicts the density of state in semiconductor as a function of energy, which is assumed to be proportional to $E^{1/2}$ above the conduction band edge and to extend exponentially below conduction band edge due to the trap states. The relative position of the Fermi levels of 2% and 10% ATO films are indicted in the diagram. The right side shows the oxidation potential of the adsorbate ground state, initial singlet excited state (prepared by 400 nm) and thermalized triplet excited state. k_i is the electron injection rate from thermalized excited state, and k_b is the charge recombination rate.

electron cross-section at 5 μm becomes almost independent of electron density, falling in a narrow range of $(2.8-3.0) \times 10^{-17}$ cm^2. As shown in Figure 3, the absorbance of the SnO$_2$ film at 5 μm is ~50 mOD, which likely contains contribution from both the absorbed water and free conduction band electrons. By attributing all the absorption at 5 μm to trap states/free carrier absorption, we estimate an upper bound of electron density of 10^{18} cm^{-3}, consistent with the expected low electron density for undoped SnO$_2$ film. Therefore, it is reasonable to assume that the electron cross-section of SnO$_2$ is around 2.8×10^{-17} cm^2.

As shown in Figure 7a, the maximum electron signal size of ReC1PO$_3$ on SnO$_2$ is ~35 mOD, whereas the signal sizes are only ~25 and ~7 mOD on 2% and 10% ATO, respectively. The measured transient IR signal size depends on the population of injected electrons, N_e, and their average IR absorption cross-section, $\sigma(\lambda)$:[9,70,71]

$$S_e(\lambda) = N_e\sigma(\lambda) \qquad (7)$$

Because the signal size has been normalized to the same number of absorbed excitation photons, assuming the same injection yield, the relative signal size should reflect the relative absorption cross-section in these films at probe wavelength (~5 μm). As listed in Table 1, the magnitudes of the calculated relative electron cross-section for the three different films agree reasonably well with the relative magnitudes of the electron signal observed. Therefore, we conclude that the variation of signal size in different films is caused by their different electron absorption cross-section.

Dependence of Forward Injection Rate on Antimony Doping Level. It appears from Figure 7b that injection rates of ReC1PO$_3$ on SnO$_2$ and ATO films are similar. This weak dependence can be understood by the small changes of accepting state density in ATO at the doping levels examined in this study. Adopting an approach similar to Marcus and co-workers, the total forward electron-transfer rate may be expressed by the sum

of electron-transfer rate to all possible accepting states of the semiconductor:[11,72−74]

$$k_{ET} = \frac{2\pi}{\hbar}\int_{-\infty}^{\infty}dE\,[1 - f(E_f,E)]\rho(E)|\overline{H(E)}|^2\frac{1}{\sqrt{4\pi\lambda k_BT}}\exp\left[-\frac{(\lambda + \Delta G_0 + E)^2}{4\lambda k_BT}\right] \qquad (8)$$

where $\Delta G_0 = E_{CB} - E_{OX}$ is the energy difference between conduction band edge and the oxidation potential of adsorbate excited state; $\overline{H(E)}$ is the averaged electronic coupling between the adsorbate excited state and different k states in the semiconductor of the same energy E (defined relative to band edge); λ is the total reorganization energy, $\rho(E)$ is the density of the semiconductor states at energy E, and $f(E_f,E)$ is the Fermi−Dirac distribution of the electrons.

According to eq 8, the forward electron injection rate is proportional to the total available accepting states in the semiconductor, which is affected by the Fermi levels of the materials. Other rate determining factors, such as electronic coupling constant, density of state and conduction band edge of semiconductor and the redox potential of adsorbate excited state, can be assumed to be independent of doping level. In principle, as the Fermi level shifts up, the available accepting states in the conduction band of semiconductor should decrease. However, the Fermi level is shifted to ~0.09 V above the conduction band edge at the 10% doping level, which is only 0.015 V higher than that of the 2% ATO sample. The redox potential of the ReC1PO$_3$ triplet state is estimated to be 0.75 eV more negative than the conduction band edge of SnO$_2$.[9] Assuming a reorganization energy of 0.3 V, the fastest injection occurs to states at 0.45 V above the band edge according to eq 7, at which the difference of available accepting states among SnO$_2$ and 2% and 10% ATO is negligible. Therefore, it is reasonable to observe similar forward injection rates from ReC1PO$_3$ to all films. It has been shown previously, as the Fermi level was shifted to a more negative value (by applying external bias), the rate of injection could be significantly retarded in TiO$_2$[18,75] and SnO$_2$[34,76] films sensitized by Ruthenium bipyridyl complexes.

Dependence of Back ET on Antimony Doping Level. Athough the forward injection rates of ReC1PO$_3$ on SnO$_2$ and ATO are the same, faster back ET is observed with the increase of the antimony doping level, as shown in Figure 7. In principle, two competing factors control back electron-transfer kinetics.[21,23,24,77] The first is the rate of ET from the trap site near the adsorbate cation and the second is the rate of electron transport in the nanoparticles. If the ET rate from the semiconductor to the adsorbate cation is much faster than electron transport, the overall recombination kinetics are controlled by the latter, which is determined by the electron trapping/detrapping rates. In the other extreme, when electron transport among different sites is fast, the recombination kinetics is controlled by the actual electron-transfer step. Many measurements indicating behaviors in either limits have been reported.[14,15,21,23,29,30,33,47,71,77−81]

In highly n-doped nanoparticles, one may expect filling of trap states and ET-rate controlled recombination kinetics. In this limit, the injection and recombination processes can be described by the following kinetics model:

$$S^*(t) \xrightarrow{k_i} S^+(t) + e \xrightarrow{k_b} S(t) \qquad (9)$$
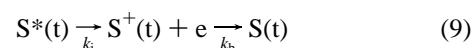
where $S^*(t)$, $S^+(t)$, and $S(t)$ represent the dye in the excited,

ET Dynamics in Re(dpbpy)(CO)$_3$Cl

J. Phys. Chem. B, Vol. 109, No. 15, 2005 **7101**

oxidized and ground states, respectively, k_i is the first-order injection rate constant from dye excited state to semiconductor forming an cation and an injected electron, k_b is the second-order rate constant for back ET, recombining a cation with a conduction band/trap electron in ATO. The changes for excited state and cation concentration are described by the following rate equations:

$$\frac{d[S^+(t)]}{dt} = k_i[S^*(t)] - k_b[S^+(t)][e]$$

$$\frac{d[S^*(t)]}{dt} = -k_i[S^*(t)] \qquad (10)$$

where [e] is the electron concentration in or near the semiconductor conduction band. For the ATO films, the electron density in the conduction band is much higher than that of the injected ones. The population of electrons can then be assumed to be constant, and the recombination step becomes pseudo-first-order in cation population with a rate constant of $k_b[e] = k_b'$. By solving eq 10, and considering that the pseudo-first-order charge recombination rate (k_b') is often much smaller than the forward electron injection rate (k_i), we obtain

$$[S^+(t)] = N_0[\exp(-k_b't) - \exp(-k_it)] \qquad (11)$$

This model suggests that in the ET control limit electron kinetics for ReC1PO$_3$ on 2% and 10% ATO can be fitted according to eq 11. To account for inhomogeneous distribution of rate constant, one can extend the single-exponential rise and decay function to multiexponential ones. If we assume that the second-order recombination rate constant k_b is independent of doping level, the pseudo-first-order decay kinetics obtained from the fit of different sample should be related by their electron concentration.

Because the recombination rate is slowest in SnO$_2$, the injection and recombination steps are well separated and the injection kinetics can be more reliably determined. We assume that the rise and decay rates from the fit can be attributed simply to the injection and recombination rates, respectively. It should be noted that we cannot exclude the possibility that minor slower rise components of injection are masked by the decay of recombination. The same biexponential rise function obtained for SnO$_2$ will be used to fit the other two samples, because, as discussed above, the forward injection rate, k_i, is unaffected by the doping levels used in this study. The recombination rate is very poorly determined in ReC1PO$_3$/SnO$_2$ because it occurs on a time scale that is significantly slower than the 1 ns observation window, whereas the recombination rate of ReC1PO$_3$/10% ATO is the fastest and can be most reliably determined. To obtain a more reliable comparison, we first fit the recombination kinetics of ReC1PO$_3$ on 10% ATO, which is well described by a biexponential decay ($A_{b,1}\exp(-t/\tau_{b,1}) + A_{b,2}\exp(-t/\tau_{b,2})$) with time constants and amplitudes of $\tau_{b,1} = 106$ ps, $A_{b,1} = 43\%$ and $\tau_{b,2} = 2032$ ps, $A_{b,2} = 57\%$. The decay kinetics of 2% ATO and SnO$_2$ are then fitted using biexponential functions with the same relative amplitudes. The rate constants differ from those of 10% ATO by a scaling factor, which is varied to achieve the best fit. This approach leads to reasonable fits of the observed kinetics, as shown by the solid lines in Figure 7b. The best-fit scaling factors, which are taken as the relative back ET rates for ReC1PO$_3$ on SnO$_2$ and 2% and 10% ATO, are shown in Table 1. It is clear that the pseudo-first-order charge recombination rate constant increases with the electron density in the conduction band of semiconductor, agreeing qualitatively with

the trend for a bimolecular recombination process. However, the effective rate constants do not depend linearly on the electron concentration. For example, the recombination rate increases by a factor of 6 from 2% to 10% ATO film, whereas the electron density only increases by a factor of 1.7. It appears that the simple model of bimolecular kinetics is not sufficient for describing the recombination process in ATO.

To understand the dependence of the recombination kinetics on doping level, more sophisticated models that take into account the transport process, such as the random flight[24] or random walk[23] model, are needed. According to the continuous-time random walk model, in materials with exponentially decaying density of trap states below the band-edge ($g(E) \sim e^{-\alpha E/kT}$), the recombination kinetics are described by stretched exponential functions and their half-lives ($t_{50\%}$) exhibit a power-law dependence on the electron population (n), $t_{50\%} \sim n^{-1/\alpha}$, when the random walker (electron) population is much higher than the target (adsorbate cation).[23] In this limit, the recombination kinetics is controlled by the distribution of trapping/detrapping time. We found that relative recombination rate in 2% and 10% ATO can be described by the above relationship with $\alpha = 0.3$. This value is similar to what was used to describe the recombination kinetics in TiO$_2$.[23] Unfortunately, the simple relationship cannot be extended to undoped SnO$_2$ because of its low and poorly determined electron concentration. Although not a proof, our finding suggests that even in doped semiconductors recombination kinetics are still affected by the trapping/detrapping kinetics.

This finding is related to previously observed dependence of back ET on the applied external bias.[20,21,47,75] Haque et al.[21,47] and O'Regan et al.[75] observed increased charge recombination rates in RuN3/TiO$_2$ at a more negative external bias. At a more negative bias, the Fermi level is raised and the population of electrons in the conduction band is increased, an effect that is similar to the increase of the doping level. The charge recombination rates were found to exhibit a power-law dependence on the electron density,[23] indicating that the recombination process was affected by electron transport processes.[22-24]

Conclusion

We have examined the doping level dependence of charge injection and recombination dynamics in ReC1PO$_3$ dye sensitized Sb:SnO$_2$ nanoparticles. Both the free carrier absorption and adsorbate vibrational spectra could be monitored by ultrafast transient IR spectroscopy. The injection rate was found to be the same in particles with 0, 2, and 10% molar percentage of Sb dopant. This is attributed to the small changes in the Fermi level in these materials, which was independently determined by modeling the IR absorption of the plasmon band. The charge recombination rates from ReC1PO$_3$ on ATO films were found to increase with the doping level. The recombination rate does not depend linearly on the concentration of doped electrons in the conduction band of ATO, demonstrating the inadequacy of the simple bimolecular model in describing the recombination kinetics and the need of a model that accounts for transport process.

7102 *J. Phys. Chem. B, Vol. 109, No. 15, 2005*

Guo et al.

References and Notes

(1) Miller, R. J. D.; McLendon, G. L.; Nozik, A. J.; Schmickler, W.; Willig, F. *Surface electron-transfer processes*; VCH Publishers, Inc.: New York, 1995.

(2) See: Michael Graetzel Festschrift.*Coord. Chem. Rev.* **2004**, *248*.

(3) O'Regan, B.; Gratzel, M. *Nature* **1991**, *353*, 737.

(4) Bach, U.; Lupo, D.; Comte, P.; Moser, J. E.; Weissortel, F.; Salbeck, J.; Spreitzer, H.; Gratzel, M. *Nature* **1998**, *395*, 583.

(5) Huynh, W. U.; Dittmer, J. J.; Alivisatos, A. P. *Science* **2002**, *295*, 2425.

(6) Hagfeldt, A.; Gratzel, M. *Chem. Rev.* **1995**, *95*, 49.

(7) Moser, J. E.; Bonnote, P.; Gratzel, M. *Coord. Chem. Rev.* **1998**, *171*, 245.

(8) Asbury, J. B.; Ellingson, R. J.; Ghosh, H. N.; Ferrere, S.; Nozik, A. J.; Lian, T. *J. Phys. Chem. B* **1999**, *103*, 3110.

(9) Asbury, J. B.; Anderson, N. A.; Hao, E.; Lian, T. *J. Phys. Chem. B* **2003**, *107*, 7376.

(10) Ellingson, R. J.; Asbury, J. B.; Ferrere, S.; Ghosh, H. N.; Sprague, J. R.; Lian, T.; Nozik, A. J. *J. Phys. Chem. B* **1998**, *102*, 6455.

(11) Asbury, J. B.; Hao, E.; Wang, Y.; Ghosh, H. N.; Lian, T. *J. Phys. Chem. B* **2001**, *105*, 4545.

(12) Benko, G.; Kallioinen, J.; Korppi-Tommola, J. E. I.; Yartsev, A. P.; Sundstrom, V. *J. Am. Chem. Soc.* **2002**, *124*, 489.

(13) Benko, G.; Myllyperkio, P.; Pan, J.; Yartsev, A. P.; Sundstrom, V. *J. Am. Chem. Soc* **2003**, *125*, 1118.

(14) Heimer, T. A.; Heilweil, E. J.; Bignozzi, C. A.; Meyer, G. J. *J. Phys. Chem. A* **2000**, *104*, 4256.

(15) Kuciauskas, D.; Monat, J. E.; Villahermosa, R.; Gray, H. B.; Lewis, N. S.; McCusker, J. K. *J. Phys. Chem. B* **2002**, *106*, 9347.

(16) Bauer, C.; Boschloo, G.; Mukhtar, E.; Hagfeldt, A. *J. Phys. Chem. B* **2001**, *105*, 5585.

(17) Hannappel, T.; Burfeindt, B.; Storck, W.; Willig, F. *J. Phys. Chem. B* **1997**, *101*, 6799.

(18) Tachibana, Y.; Haque, S. A.; Mercer, I. P.; Moser, J. E.; Klug, D. R.; Durrant, J. R. *J. Phys. Chem. B* **2001**, *105*, 7424.

(19) Tachibana, Y.; Moser, J. E.; Graetzel, M.; Klug, D. R.; Durrant, J. R. *J. Phys. Chem.* **1996**, *100*, 20056.

(20) Kamat, P. V.; Bedja, I.; Hotchandani, S.; Patterson, L. K. *J. Phys. Chem.* **1996**, *100*, 4900.

(21) Haque, S. A.; Tachibana, Y.; Willis, R. L.; Moser, J. E.; Graetzel, M.; Klug, D. R.; Durrant, J. R. *J. Phys. Chem. B* **2000**, *104*, 538.

(22) Nelson, J. *Phys. Rev. B: Condens. Matter Mater. Phys.* **1999**, *59*, 15374.

(23) Nelson, J.; Haque, S. A.; Klug, D. R.; Durrant, J. R. *Phys. Rev. B: Condens. Matter Mater. Phys.* **2001**, *63*, 205321.

(24) Barzykin, A. V.; Tachiya, M. *J. Phys. Chem. B* **2002**, *106*, 4356.

(25) Barzykin, A. V.; Tachiya, M. *J. Phys. Chem. B* **2004**, *108*, 8385.

(26) Palomares, E.; Clifford, J. N.; Haque, S. A.; Lutz, T.; Durrant, J. R. *Chem. Commun.* **2002**, 1464.

(27) Palomares, E.; Clifford, J. N.; Haque, S. A.; Lutz, T.; Durrant, J. R. *J. Am. Chem. Soc.* **2003**, *125*, 475.

(28) Clifford, J. N.; Palomares, E.; Nazeeruddin, M. K.; Graetzel, M.; Nelson, J.; Li, X.; Long, N. J.; Durrant, J. R. *J. Am. Chem. Soc.* **2004**, *126*, 5225.

(29) Hasselmann, G. M.; Meyer, G. J. *J. Phys. Chem. B* **1999**, *103*, 7671.

(30) Yan, S. G.; Prieskorn, J. S.; Kim, Y.; Hupp, J. T. *J. Phys. Chem. B* **2000**, *104*, 10871.

(31) Bauer, C.; Boschloo, G.; Mukhtar, E.; Hagfeldt, A. *Int. J. Photoenergy* **2002**, *4*, 17.

(32) Anderson, N. A.; Ai, X.; Chen, D.; Mohler, D. L.; Lian, T. *J. Phys. Chem. B* **2003**, *107*, 14231.

(33) Gaal, D. A.; Hupp, J. T. *J. Am. Chem. Soc.* **2000**, *122*, 10956.

(34) Iwai, S.; Hara, K.; Murata, S.; Katoh, R.; Sugihara, H.; Arakawa, H. *J. Chem. Phys.* **2000**, *113*, 3366.

(35) Asbury, J. B.; Wang, Y.; Lian, T. *J. Phys. Chem. B* **1999**, *103*, 6643.

(36) Anderson, N. A.; Ai, X.; Lian, T. *J. Phys, Chem. B* **2003**, *107*, 14414.

(37) Katoh, R.; Furube, A.; Hara, K.; Murata, S.; Sugihara, H.; Arakawa, H.; Tachiya, M. *J. Phys. Chem. B* **2002**, *106*, 12957.

(38) Furube, A.; Katoh, R.; Hara, K.; Murata, S.; Arakawa, H.; Tachiya, M. *J. Phys. Chem. B* **2003**, *107*, 4162.

(39) Ai, X.; Guo, J.; Anderson, N. A.; Lian, T. *J. Phys. Chem. B* **2004**, *108*, 12795.

(40) Gregg, B. A. *J. Phys. Chem. B* **2003**, *107*, 4688.

(41) Brabec, C. J. *Solar Energy Mater. Solar Cells* **2004**, *83*, 273.

(42) Granstrom, M.; Petritsch, K.; Arias, A. C.; Lux, A.; Andersson, M. R.; Friend, R. H. *Nature* **1998**, *395*, 257.

(43) Halls, J. J. M.; Walsh, C. A.; Greenham, N. C.; Marseglia, E. A.; Friend, R. H.; Moratti, S. C.; Holmes, A. B. *Nature* **1995**, *376*, 498.

(44) Schilinsky, P.; Waldauf, C.; Hauch, J.; Brabec, C. J. *Thin Solid Films* **2004**, *451−452*, 105.

(45) Yu, G.; Gao, J.; Hummelen, J. C.; Wudl, F.; Heeger, A. J. *Science* **1995**, *270*, 1789.

(46) Spanggaard, H.; Krebs, F. C. *Solar Energy Mater. Solar Cells* **2004**, *83*, 125.

(47) Haque, S. A.; Tachibana, Y.; Klug, D. R.; Durrant, J. R. *J. Phys. Chem. B* **1998**, *102*, 1745.

(48) Asbury, J. B.; Hao, E.; Wang, Y.; Lian, T. *J. Phys. Chem. B* **2000**, *104*, 11957.

(49) Wang, Y.; Asbury, J. B.; Lian, T. *J. Phys. Chem. A* **2000**, *104*, 4291.

(50) Pankove, J. I. *Optical Processes in Semiconductors*; Dover: New York, 1975.

(51) Nutz, T.; Felde, U. Z.; Haase, M. *J. Chem. Phys.* **1999**, *110*, 12142.

(52) zum Felde, U.; Haase, M.; Weller, H. *J. Phys. Chem. B* **2000**, *104*, 9388.

(53) Walters, K. A.; Gaal, D. A.; Hupp, J. T. *J. Phys. Chem. B* **2002**, *106*, 5139.

(54) Rockenberger, J.; zum Felde, U.; Tischer, M.; Troger, L.; Haase, M.; Weller, H. *J. Chem. Phys.* **2000**, *112*, 4296.

(55) Anderson, N. A.; Hao, E.; Ai, X.; Hastings, G.; Lian, T. *Chem. Phys. Lett.* **2001**, *347*, 304.

(56) Ghosh, H. N.; Asbury, J. B.; Lian, T. *J. Phys. Chem. B* **1998**, *102*, 6482.

(57) Nutz, T.; Haase, M. *J. Phys. Chem. B* **2000**, *104*, 8430.

(58) Worl, L. A.; Duesing, R.; Chen, P.; Ciana, L. D.; Meyer, T. J. *J. Chem. Soc., Dalton Trans.* **1991**, 849.

(59) Hasselmann, G. M.; Meyer, G. J. *Z. Phys. Chem. (Muenchen)* **1999**, *212*, 39.

(60) Vanhelmont, F. W. M.; Hupp, J. T. *Inorg. Chem.* **2000**, *39*, 1817.

(61) Link, S.; El-Sayed, M. A. *Annu. Rev. Phys. Chem.* **2003**, *54*, 331.

(62) Hodak, J. H.; Henglein, A.; Hartland, G. V. *J. Phys. Chem. B* **2000**, *104*, 9954.

(63) Zhang, J. Z. *Acc. Chem. Res.* **1997**, *30*, 423.

(64) Kreibig, U.; Vollmer, M. *Optical Properties of Metal Clusters*; Springer-Verlag: Berlin, 1995.

(65) Taverner, A. E.; Rayden, C.; Warren, S.; Gulino, A.; Cox, P. A.; Egdell, R. G. *Phys. Rev. B* **1995**, *51*, 6833.

(66) Button, K. J.; Fonstad, C. G.; Dreybrodt, W. *Phys. Rev. B* **1971**, *4* (3), 4539.

(67) Hunter, L. P. *Introduction to Semiconductor Phenomena and Devices*; Addison-Wesley: Reading, MA, 1966; p 31.

(68) Ashcroft, N. W.; Mermin, N. D. *Solid State Physics*; Thomson Learing: 1976.

(69) Sanon, G.; Rup, R.; Mansingh, A. *Phys. Rev. B* **1991**, *44*, 5672.

(70) Hao, E.; Anderson, N. A.; Asbury, J. B.; Lian, T. *J. Phys. Chem. B* **2002**, *106*, 10191.

(71) Weng, Y.-X.; Wang, Y.-Q.; Asbury, J. B.; Ghosh, H. N.; Lian, T. *J. Phys. Chem. B* **2000**, *104*, 93.

(72) Gao, Y. Q.; Georgievskii, Y.; Marcus, R. A. *J. Chem. Phys.* **2000**, *112*, 3358.

(73) Gao, Y. Q.; Marcus, R. A. *J. Chem. Phys.* **2000**, *113*, 6351.

(74) Gosavi, S.; Marcus, R. A. *J. Phys. Chem. B* **2000**, *104*, 2067.

(75) O'Regan, B.; Moser, J.; Anderson, M.; Gratzel, M. *J. Phys. Chem.* **1990**, *94*, 8720.

(76) Kamat, P. V.; Bedja, I.; Hotchandani, S.; Patterson, L. K. *J. Phys. Chem.* **1996**, *100*, 4900.

(77) Tachibana, Y.; Haque, S. A.; Mercer, I. P.; Durrant, J. R.; Klug, D. R. *J. Phys. Chem. B* **2000**, *104*, 1198.

(78) Kuciauskas, D.; Freund, M. S.; Gray, H. B.; Winkler, J. R.; Lewis, N. S. *J. Phys. Chem. B* **2001**, *105*, 392.

(79) Ghosh, H. N.; Asbury, J. B.; Weng, Y.; Lian, T. *J. Phys. Chem. B* **1998**, *102*, 10208.

(80) Lu, H.; Prieskorn, J. N.; Hupp, J. T. *J. Am. Chem. Soc.* **1993**, *115*, 4927.

(81) Blackbourn, R. L.; Johnson, C. S.; Hupp, J. T. *J. Am. Chem. Soc.* **1991**, *113*, 1060.